A Room Temperature Organic Polariton Transistor

Anton V. Zasedatelev[1,2], Anton V. Baranikov[1], Darius Urbonas[3], Fabio Scafirimuto[3], Ullrich Scherf[4], Thilo Stöferle[3], Rainer F. Mahrt[3], and Pavlos G. Lagoudakis[1,2]

[1]*Skolkovo Institute of Science and Technology, Moscow, Russian Federation*

[2]*Department of Physics and Astronomy, University of Southampton, Southampton, SO17 1BJ, United Kingdom*

[3]*IBM Research-Zurich, Säumerstrasse 4, Rüschlikon 8803, Switzerland and*

[4]*Macromolecular Chemistry Group and Institute for Polymer Technology, Bergische Universität Wuppertal, Gauss-Strasse 20, 42119 Wuppertal, Germany*

(Dated: February 1, 2019)

Abstract

Active optical elements with ever smaller footprint and lower energy consumption are central to modern photonics. The drive for miniaturisation, speed and efficiency with the concomitant volume reduction of the optically active area has led to the development of devices that harness strong light-matter interactions. By managing the strength of light-matter coupling to exceed losses, quasi-particles, called exciton-polaritons, are formed that combine the properties of the optical fields with the electronic excitations of the active material. Utilising polaritons in inorganic semiconductor microcavities, all-optical transistor functionality was observed albeit at cryogenic temperatures [1]. Here, we replace inorganic semiconductors with a ladder-type polymer in an optical microcavity and realise room temperature operation of a polariton transistor through vibron-mediated stimulated polariton relaxation. We demonstrate net gain of $\sim$10 dB μm^{-1}, sub-picosecond switching time, cascaded amplification and all-optical logic operation at ambient conditions.

Rapid developments in the field of strong light-matter coupling phenomena in semiconductor microcavities [2] have resulted in the emergence of a promising architecture of optical devices that range from amplifiers [3, 4], transistors [1], tunnelling diodes [5], routers [6], phase-controlled interferometers [7], ultrafast switches [8, 9] to volatile memory elements [10]. Most device concepts have been pursued on III-V semiconductors, predominantly due to the maturity of the material growth techniques and potential for electrical injection, despite the limitations imposed by the necessity for operation at cryogenic temperatures and the challenging fabrication techniques. The desire for room temperature polariton devices and the challenges posed in the growth of II-VI semiconductor microcavities [11, 12], instigated research in the field of strongly coupled organic microcavities that led to observations of polariton condensation across the visible spectrum using a broad range of organic semiconductors [13–17]. However, to exploit the advantageous properties of organic microcavities for optical devices, such as room temperature operation and ease of fabrication, it is essential to realize and enable strong non-linear processes in organic polaritonics. Here, we demonstrate the operation of a room temperature all-optical polariton transistor by utilising vibron-mediated energy relaxation and bosonic stimulation in organic microcavities. By tuning the energy of the lowest polariton state one molecular vibronic energy quantum (vibron) below the optical excitation energy, we observe the highest optical gain reported to date, $\sim$10 dB μm^{-1}. Furthermore, we realise sub-picosecond all-optical switching due to the ultrafast exciton dynamics that are inherent to organic semiconductors, demonstrate cascaded amplification and all-optical logic operation at ambient conditions.

The role of molecular vibrations in the relaxation of polaritons was theoretically investigated [18, 19] predicting their influence on the buildup of polariton population, while it was studied experimentally only in the linear regime, namely below condensation threshold [20, 21]. In inorganic microcavities, optical phonons in crystals, the equivalent of vibrons in molecular semiconductors, were shown to reduce the threshold for polariton condensation [22, 23]. Upon non-resonant injection of carriers in organic semiconductors, "hot" excitons - excitons dressed with vibrational energy - are formed, that relax predominantly through internal conversion (IC) [24]. To enable an efficient, single-step energy relaxation scheme that could potentially compete with IC, organic materials carrying vibrons with large energy and large oscillator strength are needed. Among the different organic semiconductors that have been used to realise polariton condensates, methyl-substituted ladder-type poly-

[paraphenylene] (MeLPPP) offers small homogeneous and inhomogeneous broadening due to its rigid molecular structure, and high energy vibron modes with large oscillator strength [14, 25]. Figure 1 shows a schematic of the organic microcavity used in this study. It consists of a 35 nm thick neat film of MeLPPP between 50 nm SiO_2 spacers, sandwiched between SiO_2/Ta_2O_5 distributed Bragg reflectors (DBR) on a glass substrate. Strong coupling of the cavity mode (2.65 eV) and two sub-levels of the first excited singlet state (S_{10} at 2.72 eV and S_{11} at 2.91 eV as shown in the absorption spectrum plotted on the right panel of Fig. 1) of MeLPPP result in three polariton branches exhibiting 144 meV energy splitting between the middle and the lower polariton branches (Rabi splitting), which is twice larger than the exciton-photon detuning (70 meV). To enable a single-step vibron relaxation channel in competition to IC, we select the strongest vibron available in MeLPPP ($\sim$200 meV [25]). We tune the energy of the optical excitation, accordingly, at 2.8 eV, one vibron above the lowest polariton state. Along the desired vibronic relaxation, depicted in Fig. 1 with a black solid arrow, IC results in energy relaxation from the pump-injected "hot" excitons to the lowest energy level of the first excited singlet state, S_{10} - depicted with a blue solid arrow; for the interplay between IC and vibron-mediated relaxation of pump-injected "hot" excitons see Supplementary Information (SI) Section I.

We study the excitation density dependence of polariton emission under pulsed optical excitation at 2.8 eV by means of dispersion imaging - for more information see Methods. We observe a transition from the linear to the non-linear regime at an incident excitation density of $\sim$82 μJ cm^{-2} (see SI, Section II for the method used to calculate threshold). Figure 2a shows the normalised emission from the lower polariton branch above threshold. The white dashed line is a fit to the parabolic dispersion measured in transmission below threshold, illustrating the rigid blue shift of the polariton dispersion in the non-linear regime (see SI, Section III for details). The top panel of Fig. 2b shows the emission near in-plane quasi-momentum $k_{\|} = 0$ versus excitation density, wherein the gray shaded line indicates the threshold. The top panel of Fig. 2c shows the corresponding full width at half maximum (FWHM) and the emission energy at the maximum of the emission spectrum. At threshold, we observe a collapse of the FWHM and an energy blueshift, indicative of the formation of a polariton condensate (see SI, Section IV for the linear dispersion photoluminescence images). We note that in the presence of the single-step vibron-mediated relaxation channel, the condensation threshold is more than an order of magnitude smaller than the threshold

under non-resonant optical excitation at 3.1 eV outside the DBR bandgap of the same structure under investigation here and at the same exciton-photon detuning, while the MeLPPP material absorption is only half at 3.1 eV compared to 2.8 eV.

We exploit the single-step vibron-mediated channel in the relaxation of excitons in conjunction with the occurrence of bosonic stimulation to realise a room temperature polariton amplifier. Under the excitation conditions used above, we introduce an additional optical control beam resonant to the ground polariton state that acts as a seed for triggering bosonic stimulation - for information on the experimental configuration see Methods. The excitation density of the control beam is kept constant at $\sim$20 nJ cm^{-2}, more than three orders of magnitude weaker than the non-resonant pump at 2.8 eV, adjusted to allow for its detection with our dispersion imaging apparatus in transmission configuration (see SI, Section IV for the incident and transmission spectrum of the control beam). With increasing pump excitation density, we observe a transition from the linear to the non-linear regime. The bottom panel of Fig. 2b shows the emission near $k_{\parallel} = 0$ versus excitation density, wherein the gray shaded line indicates the threshold at $\sim$49 μJ cm^{-2}. The horizontal dashed line depicts the level of the recorded intensity in the presence of the control beam only. The bottom panel of Fig. 2c shows the corresponding FWHM and the energy of the maximum intensity of the emission spectrum, where we observe a collapse of the FWHM and an energy blueshift similar to the case of the non-resonant pump-only excitation scheme. In Fig. 2d, we present the emission from the lower polariton branch above threshold. For wavevectors higher than ± 1 μm^{-1} the emission is recorded with 100 times longer integration time to allow for the measurement of the shape and rigid blueshift of the non-linear dispersion above threshold. We observe that the emission intensity is strongly concentrated on the polariton states seeded by the control beam. The right panel of Fig. 2d shows the energy distribution of polaritons revealing a highly occupied ground state coexisting with a nearly Boltzmann distribution of excited states, similar to the pump-only case shown on the right panel of Fig. 2a. This behaviour is reminiscent to a Bose-Einstein distribution previously observed in polariton and photon condensates [14, 26–28]. The spectroscopic signatures of polariton emission in the presence of an optical control beam suggest a dynamic polariton condensation [4]. Evidently, by seeding the ground polariton state, we observe nearly twice lower threshold for polariton condensation, while the exciton to polariton relaxation rate is 50-fold increased under the same non-resonant optical excitation density (see SI, Section II).

Dynamic condensation was previously observed in inorganic microcavities at cryogenic temperatures [4]. By satisfying the phase-matching conditions for pair polariton scattering, under resonant optical pumping near the inflection point of the lower polariton dispersion, stimulated polariton scattering was shown to provide large amplification of an optical seed resonant to the ground polariton state [3, 4]. Our observation of dynamic condensation in organic microcavities offers operation at ambient conditions, while removing the constraint for phase-matching of the pump with the polariton dispersion due to the localized nature of the exciton reservoir [18] (see SI, Section V). The illustration on the top panel of Fig. 3 shows the principle of a polariton transistor combining both the highly desired positive material gain for signal amplification and ultrafast operation for all-optical switching between binary logic levels. Regarding the spectral characteristics of the realised optical amplification, Fig. 3a shows a comparison of the transmission spectrum of the control beam with and without the pump, in the pump saturation regime (180 μJ cm^{-2}), demonstrating 400-fold amplification of the signal (for details of the experiment, see Methods). We note that the optical amplification is observed both in transmission and reflection geometry (see SI, Section V). To reach the maximum possible signal amplification from this structure, we study the fluence dependence of the control beam, while keeping the pump excitation density at 180 μJ cm^{-2}. In Fig. 3b we plot both the signal amplification and net gain (dB/μm) versus control beam fluence (for details of the experiment, see Methods) and observe a power-law dependence as previously reported in inorganic microcavities [3]. Notably, the signal amplification of factor 6500 obtained under ambient conditions in our work is even larger than the value reported by Saba et. al. in inorganic systems at cryogenic temperatures [4]. For the weakest accessible signal here, we record a net gain of 9.7 dB/μm, the highest reported value amongst any non-linear optical material (for a comparison see SI, Section V). Figure 3c shows the emission versus the control beam power for two different pumping conditions: below (blue open squares) and above (red dots) pump-only condensation threshold. The dependence below (above) condensation threshold is acquired for a pump excitation density fixed at $0.75P_{th}$ ($2P_{th}$). For below threshold pumping we observe the threshold dependence at control beam power of 3 nW that allows for controlled amplification between binary levels, i.e. digital signal processing. For above threshold pumping, we observe an S-shaped dependence on the power of the control beam with a threshold at 30 pW and saturation onset at 10 nW that allows for a broad range of linear amplification, i.e. analogue signal

processing.

The combination of ultrafast exciton relaxation dynamics, inherent to organic semiconductors, and the sub-picosecond cavity lifetime here, allows to configure the process of dynamic polariton condensation as an ultrafast all-optical switch. The top panel of Fig. 3 shows the principle of operation, wherein the pump beam forms the address state that is gated by the control beam. Figure 3d shows the response time of the switching from 'low' to 'high' level in the presence of the control beam by scanning the time delay between the two beams (for details of the experiment, see Methods). The total switching energy of the control beam is 1 pJ that corresponds to a fluence of 20 nJ cm^{-2}. Figure 3e shows the dependence of the extinction ratio, determined as the ratio of the intensity levels '1'/'0', on the pump excitation density. The extinction ratio reaches 17 dB when the pump excitation density approaches the spontaneous condensation threshold. Further increase of the excitation density leads to a reduction of the extinction ratio ('1'/'0') due to the contribution of the spontaneous polariton condensate emission intensity into the address state in the absence of the control beam.

Next, we test the potential of organic polariton transistors for cascadability by implementing a two-stage amplification. Figure 4(a,b) depicts schematically the realisation of two-stage cascaded amplification, wherein the condensate emission (Address 1) of the first stage is redirected onto the "chip" and amplified further by a second pump (Pump 2) (see SI, Section VI for details on the double pump-probe optical setup). Furthermore, we employ the concept of cascaded amplification to demonstrate OR and AND logic gate operation by coupling three polariton transistors on the same "chip" utilising a single pump-double probe optical setup. Figure 4c shows the principle of operation for the OR and AND gates in a microcavity, wherein the input stages I and II are the result of amplification of two separate control beams by the same pump (Pump 1). The condensate emission of the two amplified control beams are simultaneously redirected onto the "chip" at stage III that is pumped by Pump 2. For the OR gate operation, Pump 2 is adjusted to work within the saturation regime ($\sim$2Pth) of the control signal to enable amplification of either of the two outputs of stage I and II. For the AND gate operation, Pump 2 is kept below threshold ($\sim$0.9Pth), whilst by appropriate attenuation of stages I, II, we obtain sufficient contrast at the output of state III as required for the truth-functional operator of logical conjunction (see SI, Section VI). The four panels of Figures 4d and 4e show the normalised real space

photoluminescence of the three polariton transistors, comprising the OR and AND gates respectively, for the four input configurations of each gate in the order that they are listed in the corresponding truth tables of Figure 4c.

Our experiments demonstrate vibron-mediated, dynamic polariton condensation in organic microcavities at ambient conditions, enabling all-optical polariton amplification, switching at sub-picosecond time scales as well as cascadability and OR and AND logic gate operation. Efficient control over the address state permits reliable switching between 'low' and 'high' logic levels with ultrafast transient response, while the giant net gain of the structure gives rise to record optical amplification at the micrometer scale. The developed principles of dynamic polariton condensation in combination with the recently observed frictionless polariton flow in organic microcavities [29], pave the way for on-chip circuitry with ultrafast, all-optical, logic operability.

[1] Ballarini, D. *et al.* All-optical polariton transistor. *Nat. Commun.* **4**, 1778 (2013).

[2] Kavokin, A. V., Baumberg, J. J., Malpuech, G. & Laussy, F. P. *Microcavities*, vol. 21 (Oxford University Press, 2017).

[3] Savvidis, P. *et al.* Angle-resonant stimulated polariton amplifier. *Phys. Rev. Lett.* **84**, 1547 (2000).

[4] Saba, M. *et al.* High-temperature ultrafast polariton parametric amplification in semiconductor microcavities. *Nature* **414**, 731–735 (2001).

[5] Nguyen, H. S. *et al.* Realization of a double-barrier resonant tunneling diode for cavity polaritons. *Phys. Rev. Lett.* **110**, 236601 (2013).

[6] Marsault, F. *et al.* Realization of an all optical exciton-polariton router. *Appl. Phys. Lett.* **107**, 201115 (2015).

[7] Sturm, C. *et al.* All-optical phase modulation in a cavity-polariton mach–zehnder interferometer. *Nat. Commun.* **5**, 3278 (2014).

[8] Amo, A. *et al.* Exciton-polariton spin switches. *Nat. Photon.* **4**, 361-366 (2010).

[9] Gao, T. *et al.* Polariton condensate transistor switch. *Phys. Rev. B* **85**, 235102 (2012).

[10] Cerna, R. *et al.* Ultrafast tristable spin memory of a coherent polariton gas. *Nat. Commun.* **4**, 2008 (2013).

[11] Christmann, G., Butté, R., Feltin, E., Carlin, J.-F. & Grandjean, N. Room temperature polariton lasing in a GaN/AlGaN multiple quantum well microcavity. *Appl. Phys. Lett.* **93**, 051102 (2008).

[12] Lu, T.-C. *et al.* Room temperature polariton lasing vs. photon lasing in a ZnO-based hybrid microcavity. *Opt. Express* **20**, 5530–5537 (2012).

[13] Kéna-Cohen, S. & Forrest, S. R. Room-temperature polariton lasing in an organic single-crystal microcavity. *Nat. Photon.* **4**, 371–375 (2010).

[14] Plumhof, J. D., Stöferle, T., Mai, L., Scherf, U. & Mahrt, R. F. Room-temperature bose-einstein condensation of cavity exciton-polaritons in a polymer. *Nat. Mater.* **13**, 247-252 (2014).

[15] Daskalakis, K. S., Maier, S. A., Murray, R. & Kéna-Cohen, S. Nonlinear interactions in an organic polariton condensate. *Nat. Mater.* **13**, 271-278 (2014).

[16] Dietrich, C. P. *et al.* An exciton-polariton laser based on biologically produced fluorescent protein. *Sci. Adv.* **2**, e1600666 (2016).

[17] Cookson, T. *et al.* A Yellow Polariton Condensate in a Dye Filled Microcavity. *Adv. Opt. Mater.* **5**, 1700203 (2017).

[18] Michetti, P. & La Rocca, G. Exciton-phonon scattering and photoexcitation dynamics in j-aggregate microcavities. *Phys. Rev. B* **79**, 035325 (2009).

[19] Mazza, L., Kéna-Cohen, S., Michetti, P. & La Rocca, G. C. Microscopic theory of polariton lasing via vibronically assisted scattering. *Phys. Rev. B* **88**, 075321 (2013).

[20] Coles, D. M. *et al.* Vibrationally assisted polariton-relaxation processes in strongly coupled organic-semiconductor microcavities. *Adv. Funct. Mater.* **21**, 3691–3696 (2011).

[21] Somaschi, N. *et al.* Ultrafast polariton population build-up mediated by molecular phonons in organic microcavities. *Appl. Phys. Lett* **99**, 209 (2011).

[22] Deng, H. *et al.* Quantum degenerate exciton-polaritons in thermal equilibrium. *Phys. Rev. Lett.* **97**, 146402 (2006).

[23] Maragkou, M., Grundy, A.J.D., Ostatnickỳ, T. & Lagoudakis, P.G. Longitudinal optical phonon assisted polariton laser. *Appl. Phys. Lett.* **97**, 111110 (2010).

[24] Gadermaier, C. *et al.* Dynamics of higher photoexcited states in m-LPPP probed with sub-20 fs time resolution. *Chem. Phys. Lett.* **384**, 251–255 (2004).

[25] Schweitzer, B *et al.* Spontaneous and stimulated emission from a ladder-type conjugated polymer. *Phys. Rev. B* **59**, 4112 (1999).

[26] Kasprzak, J. *et al.* Bose–Einstein condensation of exciton polaritons. *Nature* **443**, 409-414 (2006).

[27] Klaers, J. *et al.* Bose–Einstein condensation of photons in an optical microcavity. *Nature* **468**, 545-548 (2010).

[28] Kammann, E., Ohadi, H., Maragkou, M., Kavokin, A.V. & Lagoudakis, P.G. Crossover from photon to exciton-polariton lasing. *New J. Phys.* **14**, 105003 (2012).

[29] Lerario, G. *et al.* Room-temperature superfluidity in a polariton condensate. *Nat. Phys.* **13**, 837-841 (2017).

FIGURES CAPTIONS

Figure 1. Organic microcavity and relevant energy levels. Schematic of the organic microcavity, consisting of 35 nm spin-coated film of MeLPPP, sandwiched between SiO_2/Ta_2O_5 distributed Bragg reflectors. Strong coupling of the cavity mode and the two sub-levels of the first excited singlet state of MeLPPP (horizontal dashed lines, S_{10} and S_{11}) resulting in three polariton branches - the upper/middle/lower polariton branch drawn in brown/green/blue color respectively versus angle. The MeLPPP absorption spectrum is plotted on the right panel vs wavelength for comparison. The optical pump is tuned to 2.8 eV injecting "hot" excitons shown as red-shaded area. Internal conversion (IC) results in relaxation of "hot" excitons to S_{10}, shown as blue-shaded area depicting a cold exciton reservoir. The exciton-cavity detuning is chosen to align the ground polariton state at one vibronic energy quantum of 200 meV below the pump injected hot excitons. Energy relaxation from the hot exciton reservoir occurs with the emission of a single vibron (black solid vertical arrow) and is seeded by the control beam tuned in resonance with the ground polariton state.

Figure 2. Spontaneous vs dynamic polariton condensation. (a) Normalised emission of the nonlinear lower polariton dispersion in the pump-only configuration at $P_{pump} = 102\ \mu J\ cm^{-2}$. The white dashed line is a parabolic fit to the measured dispersion illustrating the blue shift of the polariton dispersion in the non-linear regime. The right panel of (a) shows the corresponding energy distribution of polaritons integrated over the two- dimensional paraboloid of the lower polariton branch. (b) Emission near $k_{\|} = 0$, integrated in the range over $\pm 0.5\ \mu m^{-1}$, versus pump excitation density for the pump-only (top panel) configuration and with the additional control beam (bottom panel). The gray shaded lines indicate the respective thresholds. The horizontal dashed line in the bottom panel depicts the level of the recorded intensity from the control beam only. (c) Emission photon energy at the maximum of the emission spectrum (right/blue axis) and full width at half maximum (left/red axis) versus pump excitation density for the configurations with pump-only (top panel) and with the additional control beam (bottom panel). (d) Emission from the nonlinear lower polariton branch in the configuration of with pump and control beam at $P_{pump} = 83\ \mu J\ cm^{-2}$ and $P_{control} = 20\ nJ\ cm^{-2}$, color-scaled to allow for comparison of intensities with (a). The white dashed line is a parabolic fit to the measured data. For in-plane wavevectors

higher than ± 1 μm^{-1} the emission is recorded with 100 times longer integration time to allow for the visualisation of the shape of the non-linear dispersion above threshold. The right panel of (d) shows the corresponding energy distribution of polaritons integrated over the two-dimensional paraboloid of the lower polariton branch.

Figure 3. Characteristics of the organic polariton transistor. Schematic of an all-optical polariton transistor. (a) Measured control beam transmission spectrum with (blue) and without (black) the pump. For better visibility the non-amplified signal is shown multiplied by 200. (b) Signal amplification (left axis) and net gain (dB/μm, right axis) versus control beam fluence under constant pump at $P_{pump} = 180$ μJ cm^{-2}. (c) Emission versus control beam power for two different pumping conditions: below (blue open squares) and above (red dots) pump-only condensation threshold. (d) Transient transmission signal versus the time delay between the two beams. The FWHM of the temporal response of switching from 1 to 0 is $\sim$500 fs. The excitation density of the control beam, i.e. the switching energy, is 1 pJ. (e) Extinction ratio (ratio of the emission intensities of 1 and 0 states) versus pump excitation density.

Figure 4. Cascaded amplification and logic gates.(a) Schematic of the first amplification stage. In the absence of Pump 2, the output signal from the first stage (Address 1) produces a virtually undetectable signal at the second stage. (b) Pump 2 powers the second amplification stage of Address 1 resulting in the output signal of Address 2. (c) Schematic of an OR gate: the input stages I and II are the result of amplification of two separate control beams by the same pump (Pump 1) utilising a single pump-double probe optical configuration. The condensate emission of the two amplified control beams are simultaneously redirected onto the "chip" at stage III that is pumped by Pump 2 utilising a second single pump-double probe setup. (d) Normalised real space photoluminescence of the three polariton transistors comprising the OR gate. (e) Normalised real space photoluminescence of the three polariton transistors comprising the AND gate. The four panels of (d) and (e) correspond to the four input configurations of each gate in the order that they are listed in the corresponding truth tables of (c).

METHODS

Sample fabrication.

The sample is composed of a bottom distributed Bragg reflector (DBR), a central cavity defect region with an effective thickness slightly larger than half the exciton wavelength, and a top DBR on a fused silica substrate. The DBRs consist of alternating SiO_2/Ta_2O_5 quarter-wavelength-thick layers produced by sputter deposition (9+0.5 pairs for the bottom DBR, 6+0.5 for the top DBR). The center of the cavity consists of a polymer layer sandwiched within 50-nm spacer layers of sputtered SiO_2. The SiO_2 spacer is sputtered on the organic using a sputter target and not reactive ion sputter deposition. Methyl-substituted ladder-type poly(p-phenylene) (MeLPPP; $M_n = 31500$, $M_w = 79000$) was synthesized as described elsewhere [30]. MeLPPP is dissolved in toluene and spin-coated on the bottom spacer layer. The film thickness of approximately 35 nm is measured with a profilometer (Veeco Dektak).

Spectroscopy. The pump beam with 150-200 fs pulse duration was produced from a tunable optical parametric amplifier (Coherent OPerA SOLO) which was pumped by 1 kHz high energy Ti:Sapphire regenerative amplifier (Coherent Libra-HE). The center wavelength was adjusted with respect to experiments at 2.8 eV having 30 meV full-width at half-maximum (FWHM). The pulses were focused at the sample to a 250 μm spot with a 750 mm lens and hit the sample at 45°. Filtered broadband white-light-continuum (WLC) generated in a sapphire plate with photon energies in the range 2.47 - 2.7 eV was utilized as the control beam having 400-600 fs pulse duration. The control beam was focused on the sample at the normal incidence to 600 μm spot size with a 150 mm lens seeding the ground polariton state. About 7% of the control beam cover the spectral region corresponding to polariton states. In all measurements, temporal and spatial overlapping between the control and the pump beams were optimized by maximizing the signal of the output nonlinear emission from the sample. Temporal overlapping was varied by using a motorized translation stage with retroreflector in the control beam optical path.

Momentum-resolved emission distributions and pump-power dependences were acquired in transmission geometry. Output emission of the sample was collected with a 10X Mitutoyo plan apo infinity corrected objective (NA = 0.28) and coupled to a 750 mm spectrometer (Princeton Instruments SP2750) equipped with an electron multiplying CCD camera (Princeton Instruments ProEM 1024BX3). The emission was spectrally and in-plane

wavevector resolved using a 1200 grooves/mm grating and a slit width of 200 μm at the entrance of the spectrometer. The power of the control beam was fixed at 20 nJ cm^{-2} fluence. To obtain the incident excitation density of the pump pulse, the average pump power was measured using a calibrated Si photodetector (Thorlabs-Det10/M) and an oscilloscope (Keysight DSOX3054T) for data acquisition. Accuracy verification of the power measurements was carried out by using two independent power meters: 1 - Si photodiode power sensor (Thorlabs-S120VC) with a power meter console (Thorlabs-PM100D), 2 - thermal power sensor (Thorlabs-S302C) equipped with the power meter console (Thorlabs-PM100D).

Transmission and reflection spectra demonstrating the optical amplification effect (see Fig. 3a of the main text and Fig. S9(a,b) in SI) have been acquired by using compact fiber-coupled spectrometers. In transmission geometry, output emission of the sample was collected by a lens with 150 mm focal length through an iris restricting the collection angle within ±2° (corresponds to ±0.5 μm^{-1} in quasi-momentum space) and coupled to a fiber spectrometer (Ocean Optics Flame with 1 nm spectral resolution). In reflection geometry, the output emission of the sample was also collected by a lens with 150 mm focal length through an iris restricting the collection angle within ±2° and coupled to a fiber spectrometer (Thorlabs with 0.5 nm spectral resolution). Moreover, another fiber-coupled spectrometer (Thorlabs with 1 nm spectral resolution) was utilized for the reference measurements to minimize inaccuracies of the measurement caused by instability of WLC generation.

Signal amplification as a function of signal power (Fig. 3b) was obtained in the transmission geometry by using a collecting lens with 150 mm focal length and an iris aperture to restrict the collection angle within ±2° (corresponds to ±0.5 μm^{-1} in quasi-momentum space). The signal amplification factor has been introduced in the following way: $SA = \frac{P_2 - P_1}{P_0}$, where P_2 is the power of the transmitted signal with presence of the pump beam, P_1 is the power of the output emission induced by the pump beam itself (without seeding the ground state) and P_0 is the power of the transmitted signal in the absence of the pump beam. A hybrid photomultiplier tube (Becker&Hickl HPM 100-06) was applied to detect the weakest output signals examined during the experiment. The system was excited at 45° with a photon energy of 2.8 eV. Excitation density of 180 μJ cm^{-2} (slightly above saturation threshold) was applied to minimize measurement errors originating from pump power fluctuations and high nonlinearity of the sample above the threshold. The measurements were limited by technically unavoidable power fluctuations in the pump beam that are then strongly am-

plified by the ground state polariton stimulation, resulting in a large noise in comparison with the amplified signal on the one hand (specified as "inaccessible area in Fig. 3b), and accessible input signal beam power range on the other hand (upper boundary of the signal energy density).

The temporal dynamics of ultra-fast switching (Fig. 3d) was determined by measuring the dependence of the total emission output induced by both beams (pump and control) as a function of time interval between the beams, which was controlled through a motorized translation stage equipped with retro-reflector in the control beam optical path. The total emission output was collected in transmission geometry with the same collection conditions as described above. The pump beam was arranged in the same way as before, having 45° angle-of-incidence and 2.8 eV photon energy. The energy density of 180 μJ cm^{-2} (slightly above saturation threshold) was applied to minimize measurement errors originating from pump power fluctuations and high nonlinearity of the sample above threshold. The fluence of the control beam was fixed at 20 nJ cm^{-2}.

---

[30] Scherf, U., Bohnen, A. & Müllen, K. Polyarylenes and poly (arylenevinylene) s, 9 The oxidized states of a (1, 4-phenylene) ladder polymer. *Makromol. Chem.* **193**, 1127–1133 (1992).

DATA AVAILABILITY

All data supporting this study are openly available from the University of Southampton repository at https://doi.org/10.5258/SOTON/D0792.

ACKNOWLEDGEMENTS

The authors acknowledge the assistance of Timur Yagafarov in demonstrating the AND gate operation. This work was partly supported by the Swiss State Secretariat for Education, Research and Innovation (SERI) and the European Unions Horizon-2020 framework program through the Marie-Sklodowska Curie ITN networks PHONSI (H2020-MSCA-ITN-642656) and SYNCHRONICS (H2020-MSCA-ITN-643238) and the UKs Engineering and Physical Sciences Research Council grant EP/M025330/1 to P.G.L on Hybrid Polaritonics and the Russian Scientific Foundation (RSF) grant No. 18-72-00227 to A.Z..

AUTHOR CONTRIBUTIONS

R.F.M. and P.G.L. designed the research. A.V.Z. and A.V.B. performed the experiments and analysed the experimental data. D.U., F.S., T.S., and R.F.M. contributed to the design and fabrication of the organic microcavity. U.S. synthesised the organic material. The manuscript was written through contributions from all authors. All authors have given approval to the final version of the manuscript.

ADDITIONAL INFORMATION

The authors declare no competing financial interests.

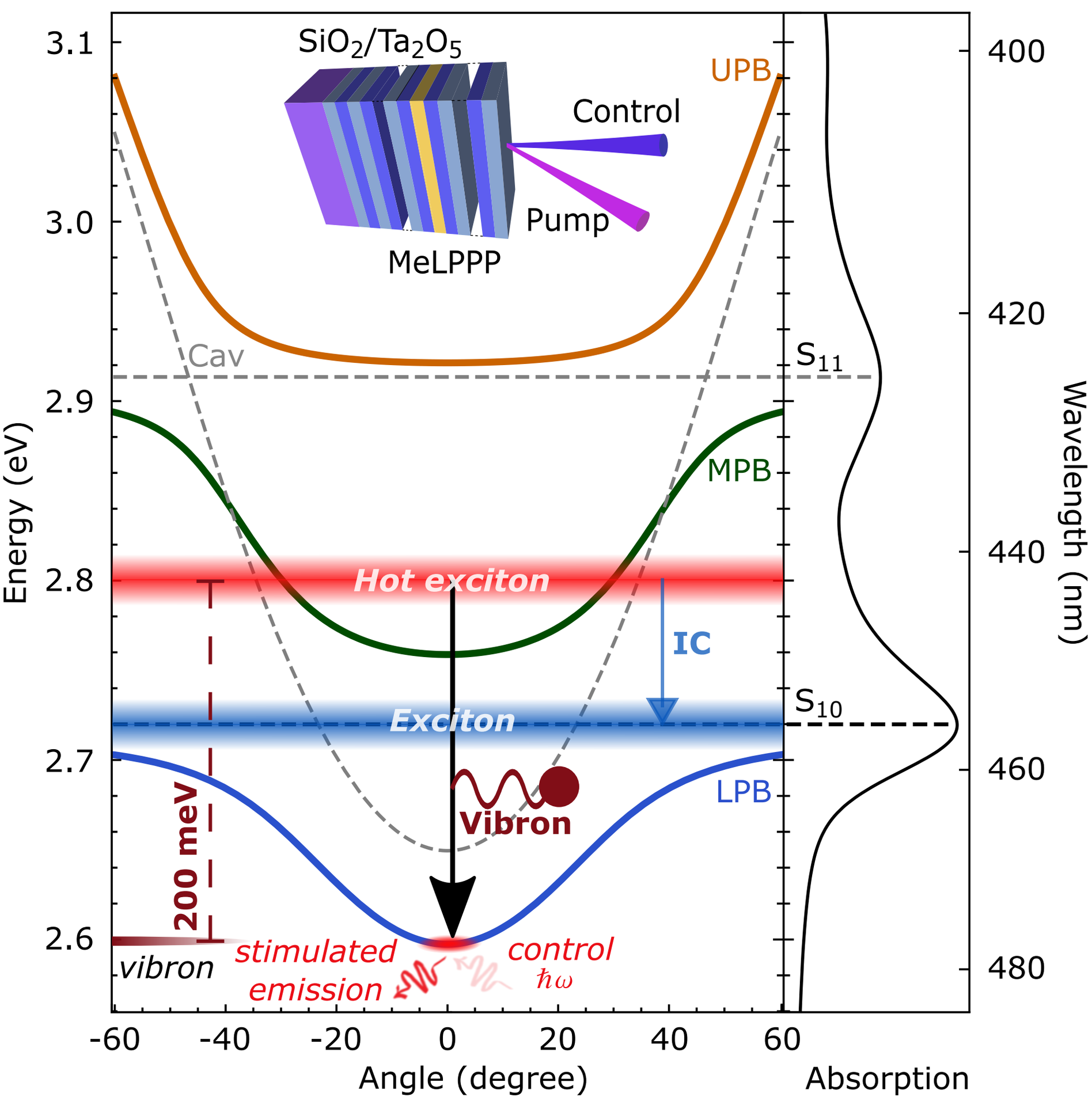
SiO2/Ta2O5
MeLPPP
Control
Pump
UPB
Cav
S11
S10
MPB
LPB
Hot exciton
Exciton
IC
Vibron
200 meV
vibron
stimulated emission
control
ħω
Energy (eV)
Wavelength (nm)
Angle (degree)
Absorption
3.1
3.0
2.9
2.8
2.7
2.6
400
420
440
460
480
-60
-40
-20
0
20
40
60

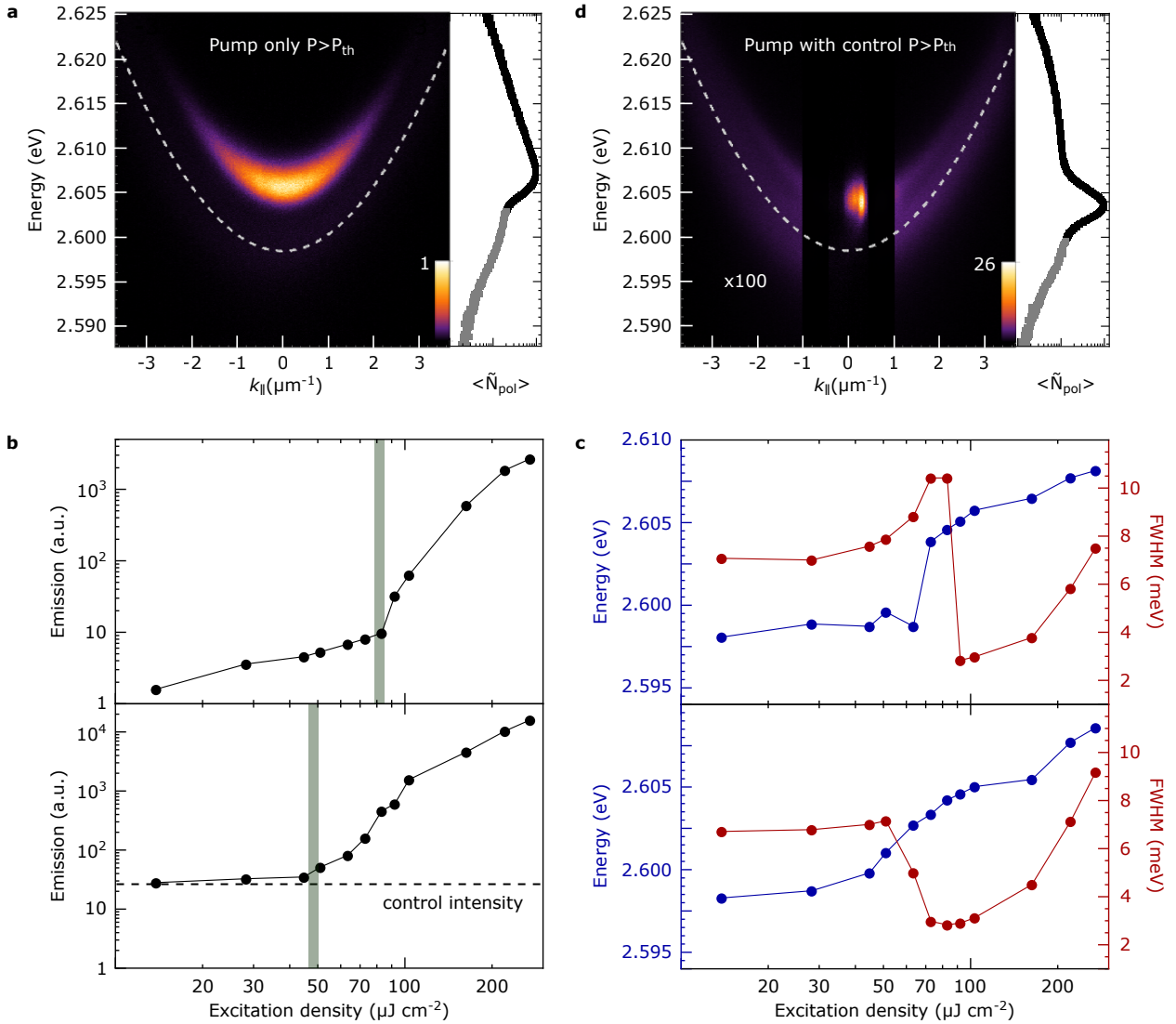
a
Pump only P>Pth
Energy (eV)
2.625
2.620
2.615
2.610
2.605
2.600
2.595
2.590
1
-3 -2 -1 0 1 2 3
k∥(μm-1)
<Ñpol>
d
Pump with control P>Pth
x100
26
b
Emission (a.u.)
control intensity
Excitation density (μJ cm-2)
20 30 50 70 100 200
c
Energy (eV)
FWHM (meV)
2.610
2.605
2.600
2.595
10
8
6
4
2

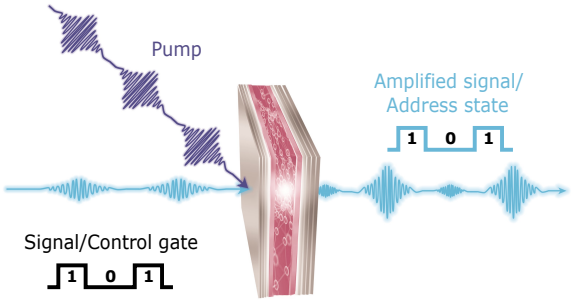
Pump
Amplified signal/
Address state
1 0 1
Signal/Control gate
1 0 1

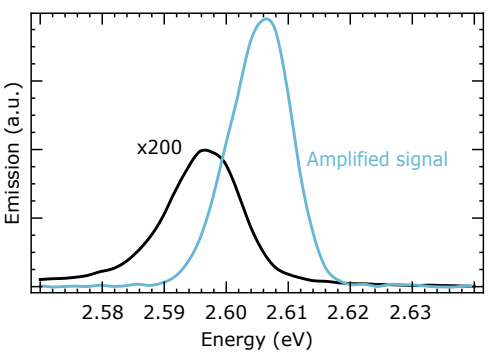
a
Emission (a.u.)
x200
Amplified signal
2.58 2.59 2.60 2.61 2.62 2.63
Energy (eV)

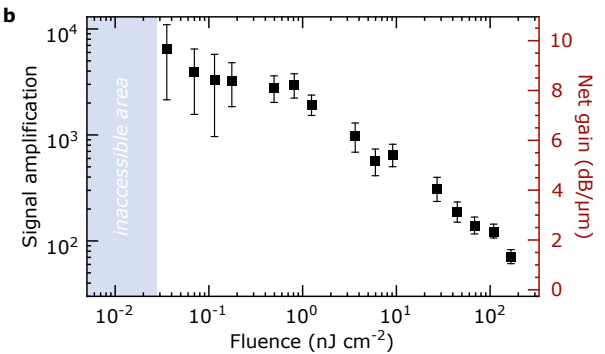
b
Signal amplification
inaccessible area
Net gain (dB/μm)
Fluence (nJ cm-2)

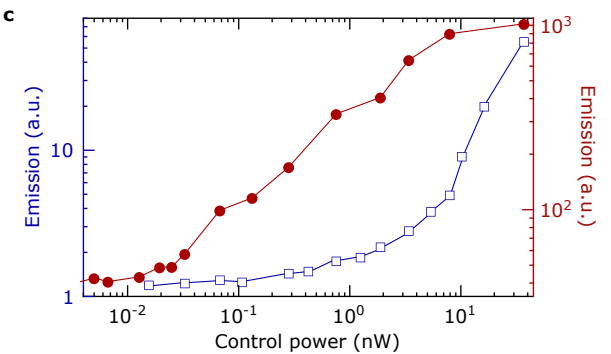
c
Emission (a.u.)
Emission (a.u.)
Control power (nW)

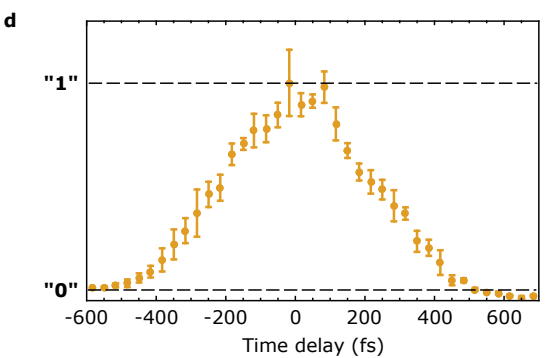
d
"1"
"0"
Time delay (fs)

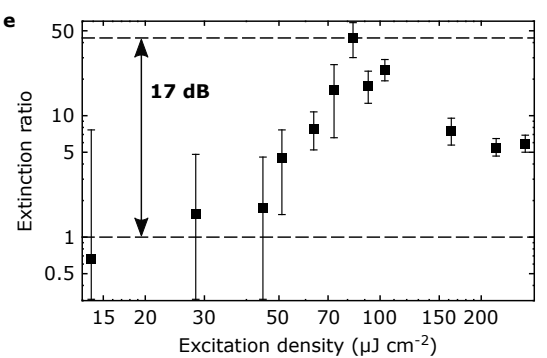
e
Extinction ratio
17 dB
Excitation density (μJ cm-2)

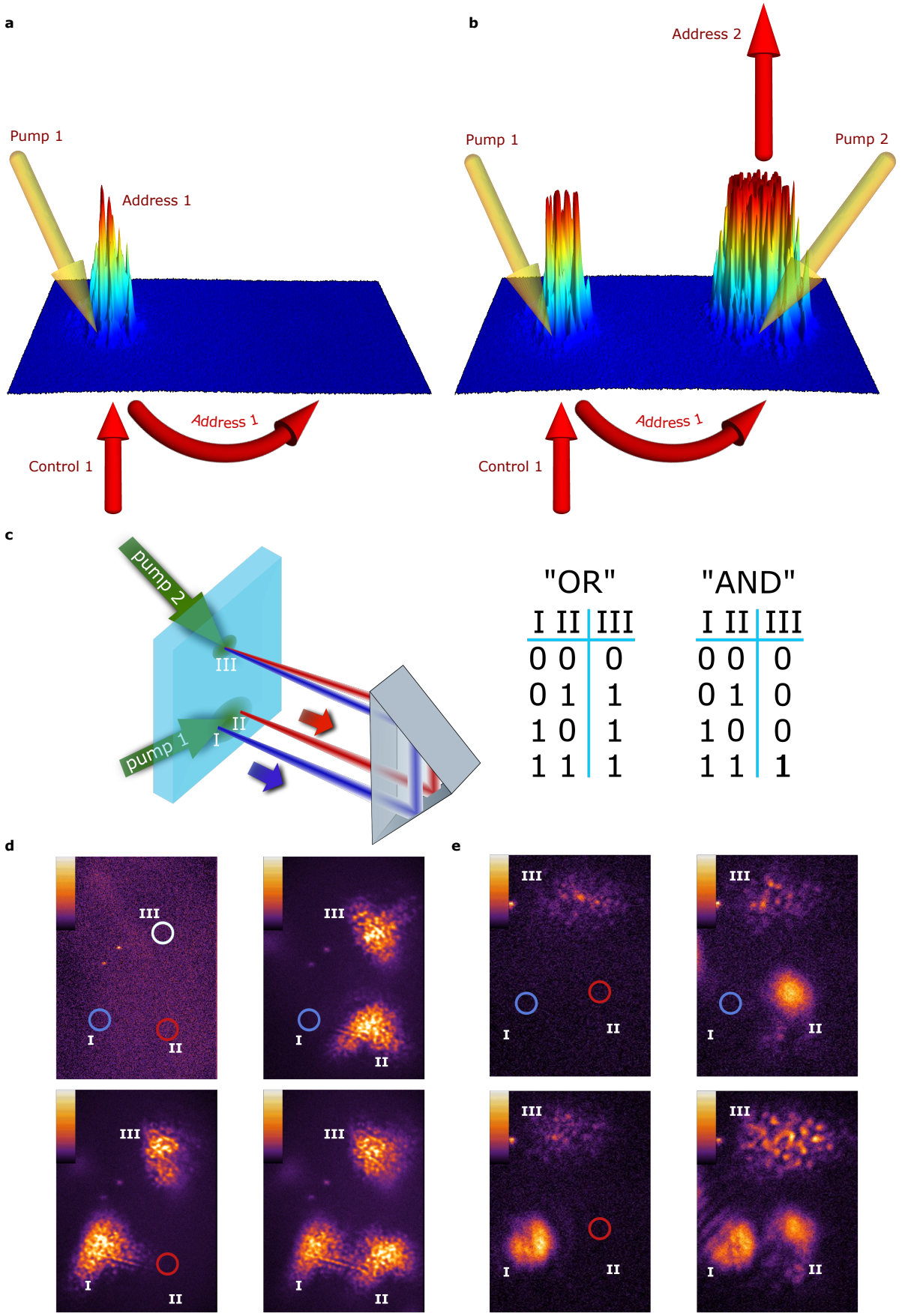
a
Pump 1
Address 1
Address 1
Control 1
b
Address 2
Pump 1
Pump 2
Address 1
Control 1
c
pump 2
pump 1
III
II
I
"OR"
I II III
0 0 0
0 1 1
1 0 1
1 1 1
"AND"
I II III
0 0 0
0 1 0
1 0 0
1 1 1
d
e